Beam emission spectroscopy for density turbulence measurements on the MAST spherical tokamak

A. R. Field,[1] D. Dunai,[2] N. J. Conway,[1] S. Zoletnik,[2] and J. Sárközi[2]
[1]*EURATOM/UKAEA Fusion Association, Culham Science Centre, Abingdon, Oxon OX14 3DB, United Kingdom*
[2]*Association EURATOM, KFKI-RMKI, P.O. Box 49, H-1525 Budapest, Hungary*

(Received 12 March 2009; accepted 14 June 2009; published online 14 July 2009)

Beam emission spectroscopy (BES) of the energetic deuterium (D^0) heating beams can provide a means of characterizing the density turbulence in tokamak plasmas. First such measurements have been performed on the MAST spherical tokamak using a trial BES system, which shares the collection optics of the charge-exchange recombination spectroscopy system. This system, with eight spatial channels covering the outer part of the plasma cross section, uses avalanche photodiode detectors with custom preamplifiers to provide measurements at 1 MHz bandwidth with a spatial resolution of 4 cm. Simulations of the measurement, including the beam absorption and excitation, line-of-sight integration of the emission spectrum, and the characteristics of the detection system have been benchmarked against the measured absolute intensity of the Doppler shifted D_α fluorescence from the 50 keV beam. This gives confidence in predictions of the performance of a two-dimensional imaging BES system planned for MAST. Correlation techniques have also provided information on the characteristics of the density turbulence at the periphery of *L*-mode plasmas as well as density perturbations due to coherent magnetohydrodynamic activity at the edge of *H*-mode plasmas. Precursor oscillations of the density in the pedestal region to edge-localized modes occurring during *H*-mode plasmas with a single-null diverted magnetic configuration are also observable in the raw signals from the trial BES system. © *2009 American Institute of Physics.*
[DOI: 10.1063/1.3170034]

I. INTRODUCTION

A. Motivation

Low-amplitude microturbulence driven by electrostatic, kinetic instabilities such as drift waves is thought to underlie the anomalously high transport rates observed in tokamak plasmas. These instabilities cause fluctuations in the plasma density, temperature, and potentials with a wide range of spatial scales, from a few ion Larmor radii, ρ_i down to the electron gyroradius, i.e., $0.01 < k_\perp \rho_i < 100$.[1] Efforts to characterize these fluctuations are aimed at establishing a link between the transport properties and the type of instability prevailing under particular conditions, e.g., ion or electron temperature gradient modes or trapped electron modes (TEM).[2] Simulations with the two-fluid, reduced magnetohydrodynamic (MHD) code CUTIE indicate that low wave number ($k_\perp \rho_i < 1$), mesoscale fluctuations, which are typically at frequencies of 0.1–1 MHz and amplitudes of $\delta n_e / n_e < 1\%$, can also lead to transport in the ion and electron thermal and momentum channels at the levels typically observed in tokamak plasmas.[3] These and other turbulence simulations show that the fluctuation amplitude decreases strongly with increasing wave number $\propto k^{-\lambda}$, where λ is of order 2. This and the fact that the resulting transport rates from mixing-length estimates scale as $\gamma_m / k_\perp^2$, where γ_m is the maximum linear growth rate, imply that large scale fluctuations could potentially result in significant levels of transport. Experimental characterization of such large scale turbulence is hence of considerable interest.

B. Measurement principle

While short wavelength turbulence ($k_\perp > 2$ cm^{-1}) can be probed using microwave or long-wavelength laser scattering,[4] these techniques are largely unsuited to probing longer wavelengths because, as $k_\perp$ is reduced, the instrumental scattering volume increases so that the turbulence cannot be localized. A diagnostic technique which is suited to the characterization of large scale density turbulence is beam emission spectroscopy (BES) on heating[5] or diagnostic neutral beams. The first method utilizes the Doppler shifted D_α emission from the energetic deuterium atoms (typically 50–100 keV) of the heating beam, which are excited primarily by collisions with the plasma and impurity ions, and hence is approximately proportional to the local electron density. Although the heating beams are quite broad [full width at half maximum (FWHM) of typically 10–20 cm] spatial localization of the order of 1 cm can be achieved by viewing the beam in a direction parallel to the magnetic field. This is because the structure of the turbulence is "flute-like" with a much longer parallel than perpendicular correlation length, i.e., $k_\perp / k_\parallel \gg 1$. By observing parallel to the field the collection volumes, which are defined by the intersection of the lines of sight with the beam, can thus be aligned to the turbulent eddies. By observing at several locations correlation analysis can be used to determine radial or poloidal correla-

tion lengths. With multichannel detectors imaged at the plasma with a radial (or poloidal) separation of 2 cm, fluctuations with wave numbers $k_{r,\theta} < 1.6$ cm^{-1} could be resolved, corresponding to $k_{r,\theta}\rho_i < 1$ for $\rho_i \sim 0.7$ cm typical of MAST plasmas. By extending the observations to two dimensions using an array of detectors it is also possible to image the density fluctuations[6] and it is planned to implement just such a system on the MAST device. A further requirement on the observation geometry is to view with an appreciable component colinear with the beam. This provides both an increase in the intersection length with the beam and, most importantly, large Doppler shifts (typically 1–3 nm) of the D_α emission from the beam atoms, which is an essential requirement to separate the beam emission from the much more intense passive D_α emission from the plasma boundary. By availing of high étendu optics to collect sufficient photons and relatively simple optical technology, i.e., interference filters and solid-state detectors, it is possible to achieve adequate signal-to-noise ratio (SNR) to measure relative density fluctuations of order 0.1% over a 100 kHz bandwidth.

C. Atomic physics considerations

The relevant atomic data required for the simulation of the beam emission are the rate coefficients for the collisional attenuation (or stopping) of the energetic deuterium heating beam and the excitation of the D_α emission through population of the $n=3$ level. At sufficiently low density, where the coronal approximation would apply, the intensity would be proportional to the plasma density. With increasing density, however, collisional excitation and de-excitation of the excited levels starts to compete with collisional excitation from the ground state and spontaneous decay in determining the population of the excited states. Because the beam atoms have velocities comparable to that of the electrons in the atomic orbitals, collisions with ions are as important as with the electrons. The nonlinear dependence of the D_α intensity on the electron density results in the relative amplitude of the intensity fluctuations $\delta I/I$ being less than that of the underlying density fluctuations $\delta n_e/n_e$. This can be quantified in terms of the differential cross section for the fractional population of the excited state j, $\kappa_j = (n_e/f_j)(df_j/dn_e)$. Estimates of using a simple collisional radiative model[5] showed that $\kappa_3 \sim 1/3$ for the $n=3$ level at moderate densities of a few 10^{19} m^{-3}. Because the relative noise level on the measured intensity depends on the inverse square root of the intensity, an order of magnitude more light must hence be collected to achieve the same sensitivity to density fluctuations than would be the case if the intensity were linearly proportional to the density.

For our calculations we use the rate coefficients for the beam stopping and excitation of the D_α line from the ADAS database.[7] Similar calculations for beam emission diagnostics were made by Hutchinson,[8] who pointed out discrepancies between the results of his calculations and those of Anderson *et al.*,[9] which underlain the relevant modules of the present release of ADAS. These discrepancies are not large, i.e., less than 10% in the rate coefficient for beam stopping and less than a factor two in the photon emission coefficients at densities below 10^{20} m^{-3}. As pointed out by Hutchinson, a much more significant effect is the influence of collisions with impurities on the rate coefficients, which is taken into account in the relevant ADAS modules. Reference 8 does however present data on the density dependence of the differential excitation cross sections κ_j, which are very useful for the interpretation of BES fluctuation data.

Data is also presented in Ref. 8 for the time constants $\tau_{2,3}$ for the equilibration of the populations of the $n=2$ and 3 excited states, which are of importance for determining the spatial resolution of beam emission diagnostics. At densities below 10^{19} m^{-3} the time constant for equilibration of the $n=3$ level is ~ 10 ns, decreasing with increasing density to 2 ns at 10^{20} m^{-3}. With the velocity of a 50 keV deuterium atom of 2.2×10^6 ms^{-1} this results in a spatial delocalization of 2.2 cm along the beam at low density decreasing to less than 0.5 cm at the higher density. As well as this fundamental limit, the spatial resolution is also limited by the line-of-sight integration through the beam and the curvature of the B-field. Using the simulation calculations presented in Sec. III, when viewing the beam from a plug-in neutral injector (PINI)-type neutral beam injection (NBI) source on MAST, this spatial delocalization is estimated to be $\sim 2-3$ cm, increasing with the observed radius.

D. Overview

A trial BES system has been installed on the MAST spherical tokamak with the aims: detecting the presence of mesoscale turbulence at the 1% level, testing electronics developed for the avalanche photodiode (APD) detectors and also benchmarking simulations of the beam emission, which are to be used to predict the performance of a more extensive BES two-dimensional (2D) imaging system planned for MAST. This trial system, which shares the collection optics of the charge-exchange recombination spectroscopy (CXRS) system viewing one of the heating beams,[10] is described in Sec. II, with particular emphasis on the APD detectors. A simulation of the BES diagnostic has been developed for the purpose of estimating the spatial resolution and SNR achievable with a particular viewing geometry, optics and detector characteristics. This is described in Sec. III along with a direct comparison of the simulated intensities with the absolute intensities measured using the trial system. This benchmarking lends confidence to any predictions based on these simulations. Some initial results from the trial system are presented in Sec. IV, including temporal and spatial correlations of large scale turbulence in L-mode plasmas, coherent MHD at the periphery of H-mode plasmas and edge-localized mode (ELM)-precursor oscillations. In Sec. V predictions of the performance of a 2D BES imaging system which is under development for implementation on MAST are presented.

II. TRIAL BES SYSTEM

A trial BES system has been implemented on MAST which shares the collection optics of the CXRS system.[10] The CXRS system has 224 spatial channels, all of which utilize the same high-throughput spectrometer. MAST is

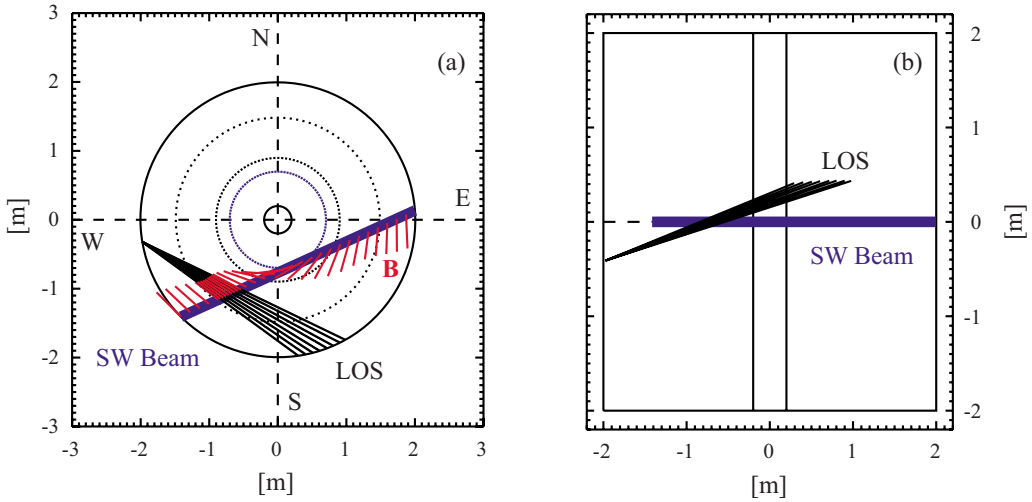

FIG. 1. (Color online) Plan and sectional views of the beam and viewing geometry for the trial BES system viewing the SW beam (shown in blue). The direction of the B-field vectors along the beam are shown in red. The dotted black circles show the locations of the magnetic axis and the outboard plasma edge and the blue circle the beam tangency radius.

equipped with two, tangentially oriented NBI heating systems, which are referred to as the SS and the SW beams. The collection optics viewing the SW beam is located at a port 0.4 m below the midplane and thus views approximately parallel to the B-field at the intersection with the beam, as shown in Fig. 1. Light from the beam is imaged by the $F/2$ collection lens onto an array of 400 μm optical fibers which relay the light to the spectrometer. The spatial channels are arranged as seven rows of 32 fibers at the input to the spectrometer. The toroidally viewing arrays shared by the BES system have 64 chords occupying two adjacent rows at the spectrometer input which cover radial ranges of 1.1 m$<R<$1.4 m and 0.8 m$<R<$1.1 m, respectively. The light from these fibers is collimated using a large aperture, commercial camera lens (200 mm, $F/1.8$) and is diffracted by a large area (100×150 mm^2) transmission grating. The grating is designed to diffract the CX emission from C^{5+} ions at 529 nm into a second lens which focuses the light onto a 2D charge coupled device detector. Conveniently, the D_α emission at ~656 nm passes undiffracted through the grating and is utilized by the trial BES system, while leaving the functionality of the CXRS system unaffected.

As shown in Fig. 2, an additional optical system located behind the transmission grating images the light onto an array of eight individual APD detectors located in a camera unit. The magnification of the optics is matched so as to image alternate pairs of the CXRS fibers onto the APD detectors, light from the intermediate pairs falling on the dead space between. This results in a spatial resolution ΔR of 4 cm over the radial range of 1.1 m$<R<$1.4 m. The first doublet L1 forms an intermediate image at a field lens L2, which is then magnified by the second doublet L3 to match the fiber images to the detector array. The light from all of the eight channels passes through a single 50 mm diameter interference filter (with central wavelength of 659 nm, 1 nm bandwidth, and peak transmission of 55%). The f-number of the light between L3 and the detectors is sufficiently large ($F/12$) so as not to broaden the bandpass function of the interference filter significantly. The main contribution to the background is the neighboring CII (657.8 and 658.3 nm) doublet. By tilting the filter the contribution from this edge emission to the core channels can be minimized. Fortuitously, the different incident angles of the light through the filter also partially match the central wavelength of the bandpass to the different Doppler shifts of the full energy D_α beam emission component, which varies with the observed radial location.

The detectors are large area APD detectors (Hamamatsu S8664–55) with 5×5 mm^2 sensitive area and high quantum efficiency (QE) of 85%. These are equipped with custom preamplifiers, which are described in detail in Ref. 11, to provide measurements at up to 1 MHz bandwidth. The out-

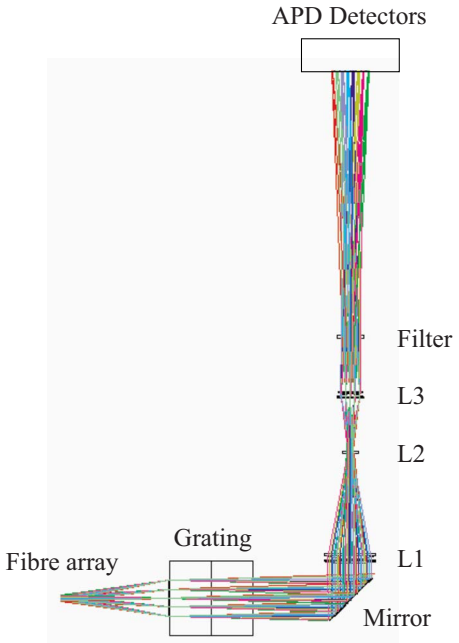

FIG. 2. (Color online) Schematic of the optical arrangement of the trial BES system, which is located on the output side of the transmission grating of the MAST multichannel CXRS spectrometer.

put voltage is digitized at 2 MHz using an eight-channel, 14 bit, 10 MHz analogue-to-digital converter (ADC) (National Instruments, PXI-6133) with a PXI host PC.

A numerical simulation of the BES diagnostic has been developed, which models the attenuation and excitation of the beam using atomic data from the ADAS database,[7] the étendu of the collection optics, filter transmission, and detector characteristics and calculates the shot noise level, both from the photon statistics and the electronics. The predicted line-integrated intensity is 4×10^{17} γ m^{-2} s^{-1} sr^{-1} for a typical channel through the beam at 1.4 MW power level, which results in $\sim3\times10^3$ detected photons in the 1 μs integration period defined by the amplifier bandwidth. The minimum level of detectable intensity fluctuations is limited by the statistical photon noise, with $\delta I/I \propto 1/N_\gamma^{1/2}$ where N_γ is the number of photons detected in the integration period. Hence, this count rate corresponds to a relative noise level of $\sim2\%$ on the measured intensity at 1 MHz bandwidth. The APD detectors have an internal gain of ~50 at 360 V bias voltage and custom, high-frequency, ultra-low-noise amplifiers are used in a temperature-stabilized housing. At 2 MHz sampling frequency the shot noise dominates the electronic noise at detected photon rates above 5×10^9 γs^{-1}. The sensitivity of the APD system to incident photons is measured to be $\sim6\times10^{-9}$ $mV/\gamma s^{-1}$.

III. SIMULATIONS

A. Introduction

A numerical simulation of the BES diagnostic on MAST has been developed to facilitate reliable predictions of the performance of a planned 2D BES turbulence imaging system. This simulation in a simplified three-dimensional (3D) geometry allows for assessment of the limitations to the spatial localization due to spatial integration effects, the temporal resolution due to photon statistics and detection noise, and the possible influence of passive impurity emission on the measurement. To do this the following processes have to be considered: the attenuation of the heating beam as it passes through the plasma; the excitation of the D_α beam emission, the line-of-sight integration of the Doppler shifted D_α emission and the passive background emission along the observation direction, the collection étendu of the optics, the transmission of the interference filters, the APD sensor characteristics and the shot noise of the photon detection, and the Johnson thermal noise of the amplifier. The noise sources of the amplifier electronics, which can dominate the shot noise in the measurements made with the trial system, are considered in a separate publication.[11] The predicted absolute intensity of the D_α emission from this simulation has been benchmarked against that measured using the trial, eight-channel BES system, thereby validating the calculations and the atomic rate coefficients used in the simulations and giving confidence in predictions of the performance of the planned upgrade.

B. Beam model

The heating beam is modeled as being axially symmetric with a Gaussian radial profile of $1/e$ half width W_b. The beam divergence is neglected because the influence of this on the measurement is small. The three energy components of the beam at the injection energy E_0 and the half-$(E_0/2)$ and third energies $(E_0/3)$ are modeled separately with power fractions f_1, f_2, and f_3, respectively, and the total power of the beam from the sum of these components is P_b. Nominal values of these beam parameters for the two available sources are given in Table I. Both of the heating beams are in the horizontal midplane with a co-current tangential orientation at a tangency radius of 0.7 m and a toroidal angle of 60° between the two beam lines. At the time of the implementation of the trial BES system the Oak Ridge National Laboratory (ORNL) source was on the SW beam at sector 6 and the PINI source on the SS beam at sector 8.

TABLE I. Nominal parameters of the heating beams used in the simulation calculations.

Source	W_b (cm)	$f_1:f_2:f_3$	E_0 (keV)	P_b (MW)
ORNL	16	77:17:6	48	1.2
PINI	8	89:8:3	75	2.5

Profiles of the electron density and temperature required for calculation of the beam attenuation and excitation were assumed to be of a simple analytic form, $f(\rho)=f_0(1-\rho^m)$, which could be matched approximately to the measured profiles. Here ρ is the normalized radius which is defined in terms of the normalized poloidal flux as $\rho=\psi_N^{1/2}$. By expressing the profiles in this way the 3D distributions can be constructed in terms of the poloidal flux, which is obtained from an EFIT equilibrium reconstruction[12] as a function of major radius and vertical position $\psi_N(R,z)$, and the assumption of axial symmetry. Nominal values used for the simulations were $T_e(0)=1$ keV with $m=3$ and $n_e(0)=4\times10^{19}$ m^{-3} with $m=4$, which gave a reasonable match to the *L*-mode profiles of discharge 17068 (at 0.28 s) for which most of the simulations were performed. The influence of impurities on the beam stopping and excitation was considered in a simplified manner by assuming a constant Z_{eff} of 1.5 and that the sole impurity is fully ionized carbon.

The attenuation of the beam is modeled by considering the loss of beam atoms during each time step Δt due to electron and ion impact ionization and charge-exchange processes. For simplicity, at this stage of the calculation, the beam flux Γ_j in each energy component j is assumed to be localized to the axis of the beam and is given in terms of the power fractions as $\Gamma_j=P_b f_j/eE_j$. The flux at the time step t_i is given in terms of the flux at the previous time step t_{i-1}, the step length along the beam Δl and the beam atom velocity v_{bj} as

$$\Gamma_j(t_i)=\Gamma_j(t_{i-1})(1-R_j\Delta l/v_{bj}), \tag{1}$$

where R_j is the rate for the beam stopping of the jth beam component. This is given by $R_j=n_e\langle\sigma\cdot v\rangle_{bs,j}$, where the rate coefficient for the beam stopping $\langle\sigma\cdot v\rangle_{bs,j}$ is obtained from the ADAS atomic database. The module ADF21 of the ADAS analysis package performs the sum over the collisional processes with the electrons, bulk deuterium ions, and

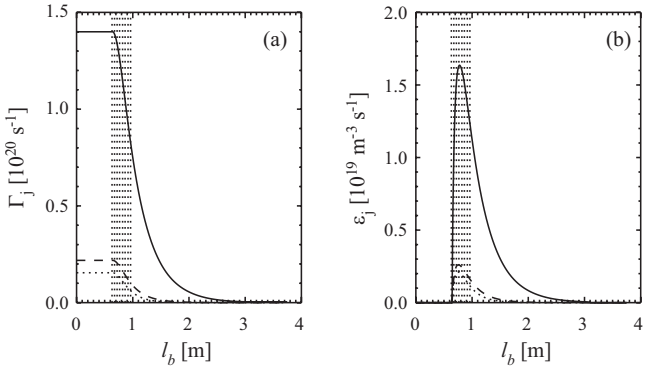

FIG. 3. Simulated profiles of (a) the beam flux Γ_j and (b) the emissivity ε_j of the D_α beam emission on the axis of the beam, where the contributions from the full (solid), half (dashed), and third (dotted) energy components are shown as a function of the distance along the beam l_b for a *L*-mode discharge heated with the SW beam injecting 1.2 MW from the ORNL source operating in deuterium at an energy of 48 keV. The viewing locations of the trial BES system are indicated by the vertical dotted lines.

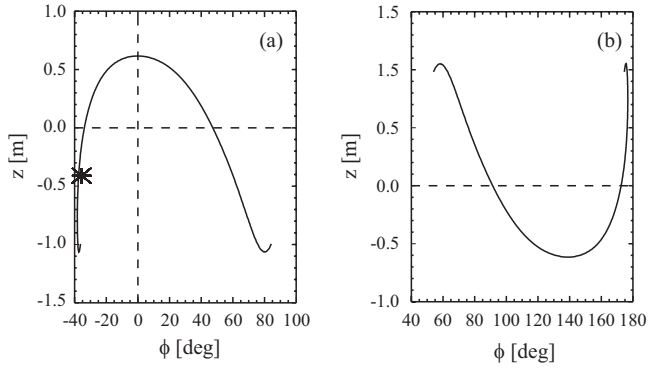

FIG. 4. Locus of optimal viewing locations at the vessel wall for (a) near, redshifted views in a direction colinear with the beam and (b) far, blueshifted views counter to the beam direction. The location of the CXRS collection optics is shown by the * symbol. The intersection of the beam axis with the wall defines the toroidal angle ϕ=0.

the carbon impurity at the appropriate density fractions specified by Z_{eff} (i.e., assuming carbon is the sole impurity) and also takes account of multistep ionization processes.

Using the simplification of a Gaussian radial beam profile and neglecting the beam divergence, the density of the beam atoms n_{bj} at a perpendicular distance r from the beam axis and a location l_i along the beam is given by

$$n_{bj}(r,l) = \frac{\Gamma_j(l_i)}{\pi v_{bj} W_b^2} \exp\{-(r/W_b)^2\}. \quad (2)$$

The emissivity of the D_α emission excited by each beam component ε_j $(r,\ l)$ at position specified relative to a location along the beam is given by

$$\varepsilon_j(r,l) = n_{bj}(r,l) n_e \langle \sigma \cdot v \rangle_{\text{ex},j}, \quad (3)$$

where the excitation rate coefficient $\langle \sigma \cdot v \rangle_{\text{ex},j}$ is obtained from the ADF22 module of ADAS in a similar way to that of the beam stopping coefficient.

Profiles of the beam fluxes $\Gamma_j(l)$ and the D_α emissivities $\varepsilon_j(0,l)$ along the axis of the beam calculated using these expressions are shown in Fig. 3 for the *L*-mode discharge specified above heated with the SW beam injecting 1.2 MW from the ORNL source operating in deuterium at 48 keV energy. In this figure the locations of the intersections of the eight lines of sight of the trial BES system with the beam are indicated by the vertical dotted lines. In the case of this *L*-mode discharge with a peaked density profile the maximum of the D_α emissivity is well aligned with the observation location.

C. Viewing geometry

For optimal spatial localization of the measurement the viewing direction has to be oriented to view along the magnetic field. Because of the flute-like nature of the turbulent fluctuations with $k_\perp / k_\parallel \gg 1$ viewing along the *B*-field will minimize the spatial averaging of the fine-scale fluctuations in the direction perpendicular to the field. At a particular location along the beam the intersection of the magnetic field vector with the vessel wall defines the optimal location for the collection optics. The two intersections in either direction forward or backward along the beam (referred to here as "near" or "far") define a locus of optimal viewing locations, as shown in Fig. 4. The Doppler shifted D_α emission from the beam would be red-shifted for the near locations viewing with the beam or blue-shifted for the far views viewing against the beam.

Because the pitch angle of the *B*-field $\alpha = B_\theta / B_\varphi$ varies strongly across the plasma in a spherical tokamak, from zero at the magnetic axis to about 40° at the plasma periphery in MAST (for a nominal plasma current of 800 kA and toroidal field of 0.48 T), there is considerable variation in the optimal viewing location depending on the observed radial location. For the near views observing the outer, low-field side as the beam enters the plasma, the optimal locations lie on an almost vertical line at a toroidal location about −38° from the center of the beam port, i.e., clockwise viewed from the top. When observing at the magnetic axis, the optimal alignment with the field is achieved for a location at the midplane or, when observing the plasma edge, from a location 1 m below the midplane. No single viewing location is therefore optimal for viewing the full radial profile and some degradation in spatial resolution is to be expected except at a particular radial location. The loci of the intersections of the magnetic field vectors with the vessel wall as a function of position along the beam are shown in Fig. 4 for cases either moving back toward the source (near) or away from the source (far). These loci thus define the optimal viewing locations for the various positions along the beam for red- or blueshifted views, respectively. The location of the CXRS collection optics is also indicated in Fig. 4 and this is conveniently optimal for viewing at the midradius region of the plasma.

D. Simulated spectra

For each of the lines of sight *k* of the simulated diagnostic, the line-integrated spectral intensity $I_{jk}(\lambda)$ of the Doppler shifted beam emission from each of the energy components *j* is calculated from

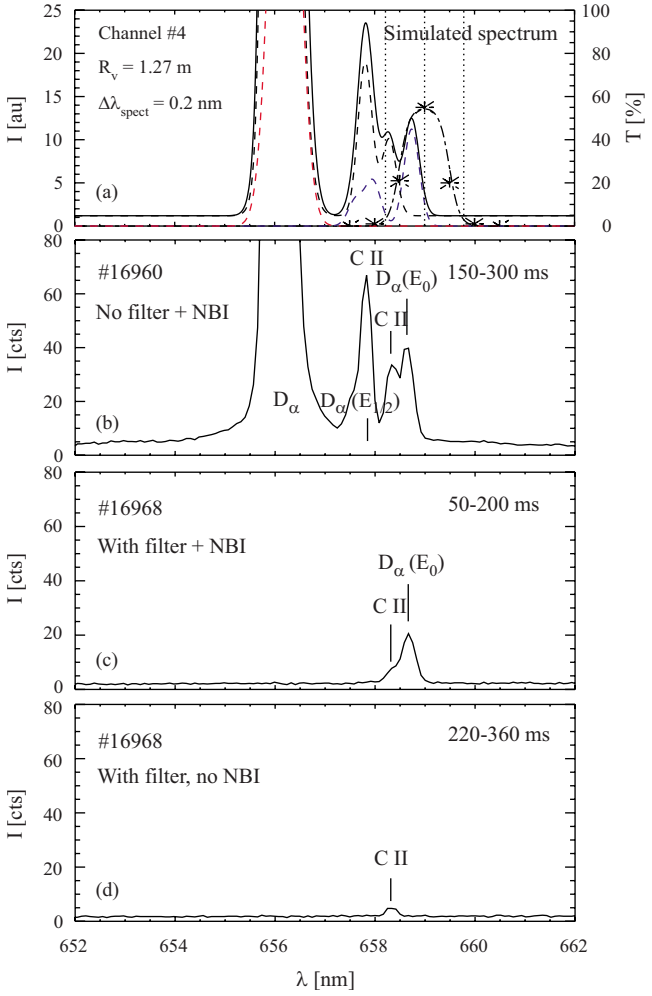

FIG. 5. (Color online) Comparison of simulated and measured spectra from channel 4 of the trial BES system viewing at a major radius of 1.27 m: (a) simulated spectrum showing the total emission (solid black), the unshifted D_α emission and the CII doublet (black dashed), the hot D_α emission (red dashed), the three components of the D_α beam emission (dashed blue) and the filter transmission (black dotted-dashed); (b) spectrum measured during NBI with no filter; (c) during NBI with filter; (d) without NBI and no filter. In these *L*-mode discharges the beam power was 1.2 MW at an injected deuterium energy of 48 keV, i.e., the same parameters as used in Fig. 3.

$$I_{jk}(\lambda) = \int I_N[\lambda_0, \Delta\lambda(v_{bj}, \theta_k)]\varepsilon_j(r,l)dl', \tag{4}$$

where l' is the location along the line of sight and $I_N[\lambda, \Delta\lambda]$ is the Gaussian line profile of the D_α line emission normalized to unit intensity and appropriately Doppler shifted for the velocity component of the beam atoms along the line of sight by wavelength, $\Delta\lambda = v_{bj}/c \cos\theta_k$, where θ_k is the angle between the *k*th line of sight and the beam direction.

What is not modeled by this simplified simulation is the emission from the secondary neutrals which are created by charge exchange between the beam neutrals and the ions of the thermal plasma or fast ions from the beam. Simulation of this so-called beam halo contribution would require a much more sophisticated calculation. Only the relatively weak emission from the neutralized fast ions, resulting in the so-called fast-ion D_α (FIDA) signal, would be expected to contribute to the intensity in the region of the direct D_α emission from the beam. Because this emission is about two orders of magnitude weaker in intensity than the direct emission from the beam atoms, it is not considered necessary to assess the contribution from this component to the measured signal for this application. The FIDA emission has however been utilized as a diagnostic for the fast-ion distribution on other tokamak devices.[13] The halo emission due charge exchange of the beam atoms with the thermal ions is crudely represented by the "hot" D_α component. This emission is however not sufficiently Doppler shifted to contribute to the intensity in the region of the direct beam emission lines.

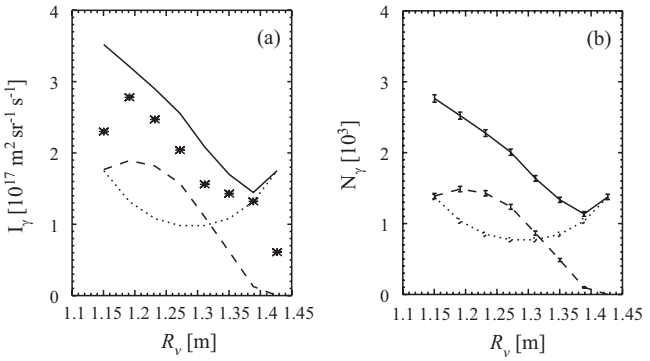

FIG. 6. A comparison of the measured (*) absolute beam emission intensity $\bar{I}_\gamma$ for the *L*-mode discharge 17068 at 0.28 s and the predicted intensity (lines) from (a) the simulation and (b) the incident photon number N_γ in an integration period of 1 μs. The separate contributions to the total (solid) from the D_α beam emission (dashed) and the background light (dotted) are shown. The same plasma and beam parameters are used as in Figs. 3 and 5.

In addition to the line-integrated beam emission, a passive contribution from the edge D_α emission and also from a CII doublet (657.8, 658.3 nm), which has an intensity ratio of 2:1, to the red side of the D_α line (656.1 nm) are added to give the total observed intensity. The passive D_α emission can also be represented approximately as the sum of a "cold" unshifted component of FWHM $w_\lambda \sim 0.17$ nm and a "hot" component from edge charge-exchange emission of $w_\lambda \sim 0.5$ nm, which is rotating with the edge plasma and hence Doppler shifted by $\Delta\lambda \sim 0.1$ nm in the cobeam direction. A constant background light intensity is also included to represent bremsstrahlung and other impurity emission. The total simulated spectrum is thereby given by

$$I_k(\lambda) = \sum_j I_{jk}(\lambda) + I_{D_\alpha}^{\text{cold}}(\lambda) + I_{D_\alpha}^{\text{hot}}(\lambda) + I_{\text{CII}}(\lambda) + I_{\text{BG}}. \tag{5}$$

The intensity of the beam emission coefficients is calculated absolutely while that of the other components is adjusted to match a measured spectrum, which is first normalized to match the intensity of the simulated beam emission components. Figure 5 shows a simulated spectrum from one of the channels of the trial BES system for the same parameters, as used for Fig. 3, i.e., for the ORNL source at 48 keV, which also shows the transmission of the interference filter $T_{\text{filt}}(\lambda)$ used to filter out the beam emission from the background light. The spectrally integrated intensity of the light passing through the filter is given by

$$\bar{I}_k = \int T_{\text{filt}}(\lambda) I_k(\lambda) d\lambda. \quad (6)$$

This is shown as a function of the channel position in Fig. 6(a).

E. Absolute signal levels

The amount of light entering the collection optics is determined by the étendu $\Delta\xi = \Delta A \Delta\Omega$, where ΔA is the light collection area and $\Delta\Omega$ is the accepted solid angle at some location along the light path. In the case of the CXRS collection optics this is defined by the effective area of the collection fibers and the f-number with which the fibers are illuminated by the collection lens. Each of the trial BES channels combines the light from two of the 400 μm diameter fibers of the CXRS system, which are filled by the collection lens at $F/2$. The effective collection area of the fibers ΔA_f is defined by their diameter D_f and the width of the slits W_s of 200 μm, which define the entrance aperture of the CXRS spectrometer, approximately as $\Delta A_f = D_f W_s$, resulting in an overall étendu of the system of $\Delta\xi$ of 3.1×10^{-8} m^2 sr.

In the trial BES system, an interference filter of 1 nm bandwidth, which is located before the APD detectors, is used to filter out the full energy component of the D_α beam emission from the other plasma light. The transmission function of this filter is shown in Fig. 5, where the wavelength shift due to the slightly off-normal incidence angle, which is different for each channel, is accounted for. The peak transmission of this three-cavity filter is 55% and it has an out-of-band blocking factor of $\sim 10^{-4}$. An estimate for the overall transmission of the optical system including losses in the fibers, the transmission of the CXRS grating and the reflections at the optical surfaces but *excluding* the filter transmission is $T_{\text{opt}} \sim 0.25$. The photon rate $\Gamma_{\gamma k}$ entering the kth channel and passing through the filter is given by $\Gamma_{\gamma k} = \Delta\xi \bar{I}_{\gamma k}$. In the case considered here the maximum photon rate is 1.1×10^{10} s^{-1}. The number of photons incident on the APD detectors in an integration period Δt is then given by $N_{\gamma k} = T_{\text{opt}} \Gamma_{\gamma k} \Delta t$, where Δt is determined by the preamplifier bandwidth B by $\Delta t = 1/B$. This is shown as a function of the observed radius in Fig. 6(b) for an integration period of 1 μs corresponding to a 1 MHz bandwidth, where the maximum incident photon number is 2.8×10^3.

The output voltage of the APD preamplifier V_{out} is given in terms of the incident photon current $i_\gamma = eT_{\text{opt}}\Gamma_\gamma$ as $V_{\text{out}} = GeM_{\text{APD}} Q_{\text{eff}} i_\gamma R_L$, where M_{APD} is the internal gain of the APD, Q_{eff} is the QE, R_L is the load resistance of the transimpedance amplifier, and G is the gain of the second stage. For the trial BES system the appropriate values are $M_{\text{APD}} \sim 50$, $Q_{\text{eff}} \sim 0.85$, $R_L \sim 50$ kΩ, and $G \sim 100$. With a maximum incident photon rate of 1.1×10^{10} s^{-1} this gives an output voltage of 95 mV, which is close to the measured value of 76 mV. The simulated and measured output voltages are shown in Fig. 7(a) as a function of the channel location. Note that the internal gain of the APD detectors can vary by a factor ~ 2 between channels, hence the variability of the discrepancy between the simulated and measured voltages.

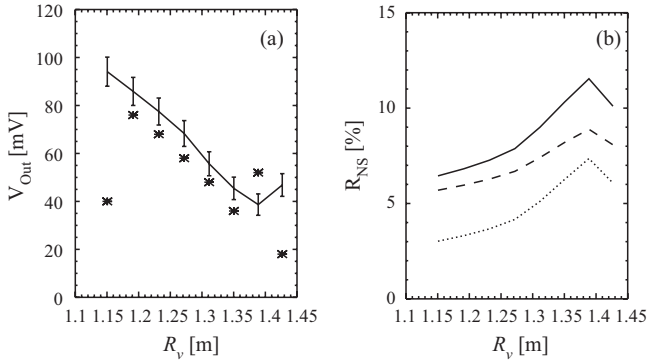

FIG. 7. The measured (*) and predicted output voltage V_{out} (solid) of (a) the preamplifiers and (b) the noise-to-signal ratio R_{NS} as a function of the channel position. The separate contributions to the total noise level (solid) from the D_α beam emission (dashed) and the background light (dotted) are shown. The same plasma and beam parameters are used as in Figs. 3 and 5.

F. Noise levels

The noise on the output voltage of the system arises from the superposition of various sources: the shot noise on the incoming photon flux ($\propto N_\gamma^{1/2}$), the statistical noise of the APD gain process, the Johnson noise of the load resistor ($\propto \sqrt{T_R R_L}$), and noise sources internal to the first amplifier stage. The noise introduced by the APD gain has statistical properties which are indistinguishable from the photon statistical noise therefore it can be considered as an effective reduction in the QE of the detector. This is taken into account by the excess noise factor F_n in Eq. (7) used for the calculation of the shot noise discussed below.

The shot noise voltage V_n is calculated by adding the contributions from the noise in the detection and amplification processes at the APD detector V_{sh} and the thermal noise in the load resistor V_{th} in quadrature. The detector shot noise is made up of that due to the fluctuations in the detected photon count $\propto \sqrt{N_\gamma}$ and amplification process and in the leakage current i_{DS}, which is ~ 4 nA and hence negligible for the S8664-55 APD. The shot noise from the APD is hence given by

$$V_{\text{sh}} = R_L (2ei_\gamma B M_{\text{APD}}^2 F_n + 2ei_{\text{DS}} B)^{1/2}, \quad (7)$$

where B is the amplifier bandwidth. The noise factor F_n is due to additional random fluctuations in the amplification process in the APD and is given approximately by $F_n = M_{\text{APD}}^x$, where x is the excess noise coefficient ~ 0.3. In addition to this the thermal noise from the load resistor, which is independent of the incident photon flux, is given by $V_{\text{th}} = \sqrt{4k_B T_R B R_L}$, where k_B is Boltzmann's constant and T_R is the absolute temperature of the load resistor. The predicted relative shot noise level $R_{\text{NS}} = V_n / V_{\text{out}}$ calculated from these contributions is shown in Fig. 7(b) for the trial BES system and has a minimum level of 6%. The actual signal and noise levels determined during a MAST L-mode discharge are shown in Fig. 8. The maximum signal level is 40 mV, decreasing with increasing radius, whereas the fluctuation level, which is dominated by the internal amplifier noise is fairly constant at 8 mV. The actual relative noise level $R_N = V_n / V_{\text{out}}$ therefore has a minimum level of $\sim 20\%$ increasing with decreasing signal level, which is considerably larger

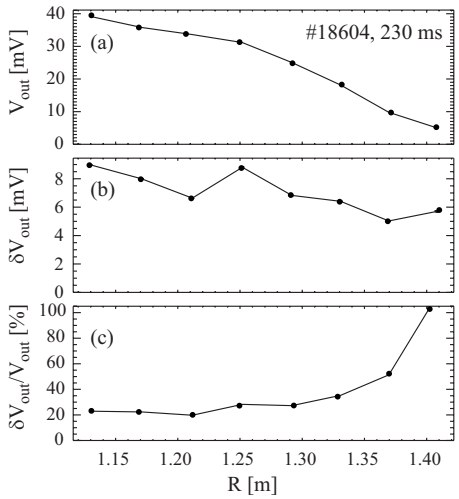

FIG. 8. Profile data from the trial BES system measured during a *L*-mode discharge showing: (a) the mean output voltage, V_{out}, (b) the absolute rms fluctuation amplitude, δV_{out}, and the relative fluctuation level, $\delta V_{out}/V_{out}$, as a function of radial channel location.

than the shot noise level at this level of incident photon flux.

The overall noise level of the system is a nonlinear function of several parameters: the detector gain, the load resistor, and the capacitances of the amplifier circuit. The latter includes the capacitance of the detector which is dependent on the applied voltage. As the value of the load resistor and the capacitors are interrelated by the required bandwidth it is not possible to adjust these parameters independently. A detailed model has been developed for the electronics which can be used to optimize the SNR at a given input photon flux. It is important to note that the settings will be optimal for only one photon flux and presently the system is optimized for the peak photon flux observed with the same parameters for all channels. Details of the amplifier modeling and optimization of the SNR are to be presented in a separate publication.[11]

Using an integrating-sphere light source of an absolutely calibrated spectral radiance $R(\lambda)=hc/\lambda I(\lambda)$ it was possible to determine the sensitivity S_γ of the APD detectors in terms of output voltage for a given incident photon rate $S_\gamma = V_{out}/\Gamma_\gamma$, which was measured to be typically $\sim 4-8 \times 10^{-12}$ V/γs^{-1}. This sensitivity could then be used to calculate the absolute intensity of the measured light emission from the plasma for comparison with the simulated values. Such a comparison is shown in Fig. 6(a) where the calculated intensities are seen to be only slightly higher than those measured by $\sim 10\%$. Considering the complexity of the simulations and the many simplifying assumptions this agreement is acceptable. In particular, the actual gain of the APD detectors is assumed to be a fixed value of 50; however this value is not known precisely and can vary by a factor ~ 2 from one device to another. As shown in Fig. 7(a), there is a similar discrepancy between the measured and calculated output voltages. This benchmark of the simulations lends confidence to any predictions of the performance of future systems based on these calculations.

For the 2009 experimental campaign the SW beam line has been upgraded with the installation of a JET-style PINI type of source with reduced beam divergence and hence greater brightness at a given power than the original ORNL "duo-pigatron" source. The new source is also able to operate at higher power than the original one. The predicted maximum photon count with the PINI source operating at 75 keV injection energy and 2.5 MW power is 6.5×10^3 γ in 1 μs, i.e., a factor 2.3 greater than with the ORNL source operating at 1.2 MW. This results in a predicted output voltage of up to 200 mV and a lower relative shot noise level of 4%, i.e., 8 mV, which will thus equal the intrinsic amplifier noise level at this photon flux.

G. Spatial resolution

If the line of sight is not exactly aligned with the *B*-field over the region where the line of sight and the beam emission intersect, then the spatial resolution of the system will be degraded. Here the additional delocalization due to the finite étendu of the optics is not accounted for because this is small compared to that due to the width of the beam. Under this assumption, the extent of the emission region along the line of sight is given by $\Delta l_\varepsilon \approx 2W_b/\sin\theta$, where $\theta \sim 45°$ is the angle between the line of sight and the beam. With the SW beam and the ORNL source Δl_ε is typically ~ 40 cm. The spatial smearing due to the deviation of the field line from the line of sight within the observation volume can then be estimated from the perpendicular distance ΔX_ε of the field line from the line of sight at the $1/e$ points of the emissivity along the line of sight, which is given approximately by $\Delta X_\varepsilon \approx \Delta l_\varepsilon \sin\beta$, where β is the angle between the line of sight and the *B*-field at the axis of the beam. For the trial BES system viewing the SW beam from the ORNL source this smearing is approximately constant at $\Delta X_\varepsilon \sim 6$ cm across the viewed region of 1.1 m $< R <$ 1.4 m, compared to the channel separation of $\Delta R \sim 4$ cm. Now that this SW beam line has been upgraded from the ORNL to a PINI source with a more collimated beam this smearing is reduced considerably to less than 3 cm across the viewed region.

For detailed interpretation of measurements from a 2D BES imaging system a full calculation of the 2D spatial smearing in radial and poloidal directions is required. Such a calculation was performed for the BES imaging system on DIII-D (Ref. 6) by Schafer *et al.*,[14] which also take account of the finite étendu of the collection optics and the lifetime of the excited state. This is characterized in terms of the point spread function $P(\mathbf{x})$ or its Fourier transform, the spatial transfer function, $\tilde{T}(\mathbf{k})=F\{P(\mathbf{x})\}$. The latter is a measure of the response of the system to density fluctuations in wave number space. The simulation calculations described here are currently being extended to calculate these quantities for the MAST BES system. This information will allow the spatial instrument response to be deconvolved from future 2D measurements and is also required for calculation of synthetic measurements from turbulence simulations for comparison with measurements.

IV. RESULTS

The trial BES system on MAST was developed primarily with the aim of testing the detector system and bench-

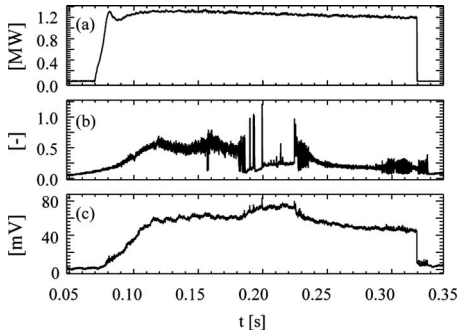

FIG. 9. Evolution of (a) SW NBI power, (b) D_α intensity and (c) beam emission intensity from channel 3 during discharge 17068 exhibiting *L*- and *H*-mode phases.

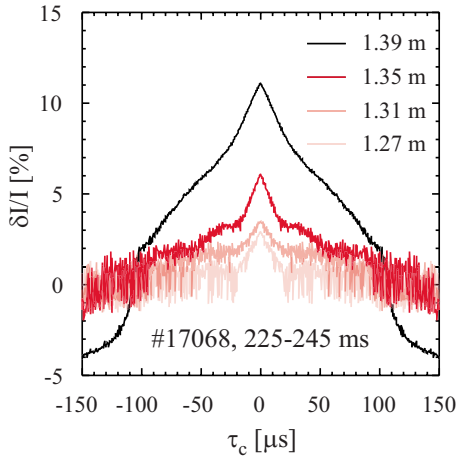

FIG. 10. (Color online) Square root of the autocovariance of BES signals normalized with the signal level from channels 2–5 during a *L*-mode phase of the discharge shown in Fig. 9.

marking the simulations of the diagnostic. By availing of the existing collection optics of the CXRS system, which views from the required location, it was possible to implement the system relatively quickly and cheaply. The relatively low étendu of the optics does however limit the resolution in terms of the relative fluctuation amplitude to ~2%. In spite of this the results presented below illustrate the potential of BES to observe both density fluctuations due to turbulence and coherent MHD activity in the core and edge plasma of MAST.[15]

The evolution of the beam emission signal from an edge channel is shown in Fig. 9 for a discharge with 1.3 MW NBI heating power. At the beam cutoff time the beam emission intensity is also seen to decrease rapidly, which is the signature of the prompt beam fluorescence. The signal level of 20–80 mV corresponds to an observed intensity in the range $1-3\times10^{17}$ γ m^{-2} s^{-1} sr^{-1}. The observed intensity typically 10% less than that predicted by the simulation of the BES system. At this measured photon rate the internal noise sources of the amplifiers of about 8 mV dominates over the photon shot noise. The residual intensity observed immediately after the NBI cutoff represents the level of background light observed in the signal which is typically 5%–10% of the total signal level.

Radial profiles of the mean output signal, together with the absolute and relative fluctuation amplitudes are shown for a *L*-mode plasma in Fig. 8. Analysis of the correlation functions and power spectra reveals that the fluctuations are dominated by broadband detector noise, which is uncorrelated between channels. This noise level is everywhere above the expected fluctuation level of the beam emission due to the density fluctuations. However, because the bandwidth of the noise is much broader than the frequency band of the density fluctuations, correlation analysis techniques[16] can be used to remove the noise and determine the level of any underlying correlated fluctuations in the signal. By calculating the temporal auto- or cross correlations of the signals over a period T of 10–100 ms, i.e., much longer than the integration period, the effective SNR can be increased at the expense of losing temporal information. From such analysis the characteristic decorrelation time τ_c, relative fluctuation amplitude levels and the radial propagation delay of turbulent structures can be extracted. The covariance of signals $\tilde{S}_i(t)$ from two channels is defined by $C_{ij}^S(\tau)=\int_0^T \tilde{S}_i(t)\tilde{S}_j(t+\tau)dt/T$, where the intensity distribution can be written as a sum of an average and a fluctuating part, $S(t)=S^0+\tilde{S}(t)$. The square root of the autocovariance of selected radial channels normalized to the mean signal level is shown in Fig. 10 for the later *L*-mode phase of the discharge shown in Fig. 9. In the outermost channel, observing just inside the separatrix, relatively high-amplitude structures with $\delta I/I \leq 10\%$ are observable with a long decorrelation time of $\tau_c > 100$ μs. At the low densities characteristic of the *L*-mode edge plasma ($\leq 10^{19}$ m^{-3}) the proportionality between the relative intensity to the relative density fluctuations is closer to unity than the factor 1/3 more appropriate for moderate densities. These fluctuations therefore correspond to a relative density fluctuation level of approximately $\delta n_e/n_e \sim 10\%$ in the periphery of the *L*-mode plasmas.

The characteristics of the edge turbulence change strongly in the *H*-mode phase of the discharge. Density perturbations of ~10% amplitude produced by coherent MHD activity at ~5 kHz are frequently observed in the edge channels. Superimposed on this, turbulent fluctuations with ~2% amplitude and correlation time $\tau_c \sim 20$ μs can be observed. In the core plasma, low amplitude ($\delta I/I \sim 1-2\%$) structures with a correlation time of $\tau_c \sim 5-20$ μs are observed, with an amplitude close to the detection limit. Intensity fluctuations of a similar character are also observed in all channels when the beam is fired into a gas target, which are produced by fluctuations in the ion current from the beam source. Attempts to remove this common-mode component from the signals have so far been unsuccessful due to the relatively high level of electronic noise from the preamplifiers. Recent measurements on the beam from the new PINI source fired into a gas target do not exhibit these common-mode fluctuations in the beam density from this source.

Multichannel, normalized cross correlations of the signals relative to a specified reference channel are shown in Fig. 11 from the *L*-mode phase of a discharge. The time lag of the fluctuations in the outermost channel (1), which is 4 cm outside the separatrix, relative to the next channel, which

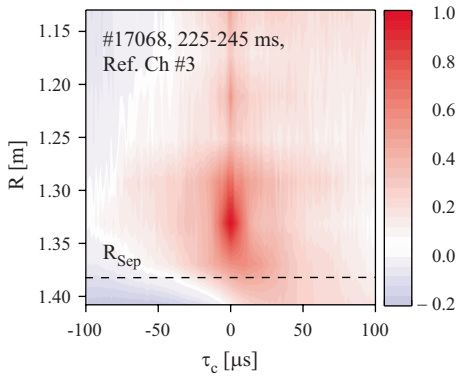

FIG. 11. (Color online) Multichannel, normalized cross correlation of BES signals from a *L*-mode phase of the discharge shown in Fig. 9. The separatrix position is indicated by the dashed line.

is at the separatrix, is evidence of an apparent outward radial propagation of the scrape-off layer (SOL) turbulence at an estimated velocity of ~ 2 km/s.

Data from an ELM-free phase of a *H*-mode discharge with enhanced D_α (EDA) emission from the upper *x*-point region is shown in Fig. 12, where the BES signals are correlated with a high-frequency Mirnov magnetic pickup coil signal instead of data from one of the BES channels. A quasicoherent mode at ~ 150 kHz is present in both the edge density and the magnetic signal. The strongest correlation of the BES signals with the magnetic signal is observed for channel 2, which localizes the mode to the *H*-mode pedestal region just inside the separatrix ($r/a \sim 0.98$). Such quasicoherent MHD modes at similar frequencies have been observed in so-called EDA *H*-modes on Alcator C-Mod tokamak[17] and in high-density *H*-mode on the Wendelstein 7-AS stellerator.[18] On C-Mod the EDA *H*-mode is thought to be due to a high poloidal mode number ($m \sim 100$) resistive ballooning mode localized near the *x*-points which occurs in high-density, high collisionality operation. The density pump-out observed on C-Mod, which is due to degradation of the particle confinement in the presence of this mode, causing a saturation of the line-averaged density is not however observed on MAST, the density still increasing during the *H*-mode phase in the presence of this mode.

Precursor oscillations of the density in the edge pedestal

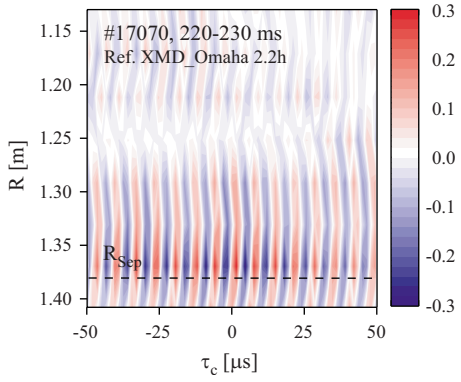

FIG. 12. (Color online) Multichannel, normalized cross correlation of BES signals with a high-frequency (>20 kHz) Mirnov coil signal from the outboard midplane during an ELM-free phase of a high-recycling NBI heated *H*-mode discharge. The separatrix location is indicated by the dashed line.

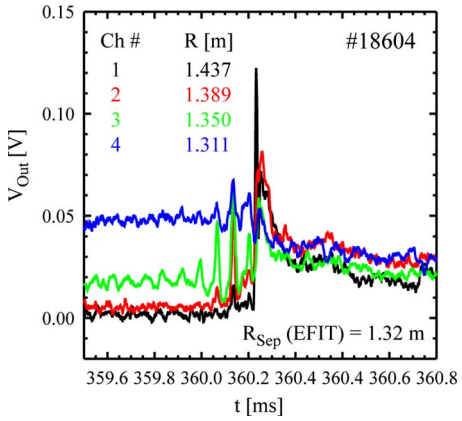

FIG. 13. (Color online) Beam emission signal from the outermost four channels of the trial BES system shown evidence for ELM precursor oscillations of the density in the pedestal region of a NBI heated *H*-mode discharge with a L-SND magnetic configuration.

region prior to the occurrence of ELMs can also be observed in the raw signals from the BES system, as shown in Fig. 13. This discharge was in a strongly shifted, lower single-null diverted (L-SND) magnetic configuration and was heated by 1.5 MW of NBI power, which was consequently deposited off-axis. These results are discussed in more detail in Ref. 19. The precursor is apparently related to a low mode number core MHD mode which is observed to evolve outward toward the edge. It is thought that this may then modify the pressure gradient there, triggering the fast-growing fingerlike mode observed in the BES data, which destabilizes the pedestal and finally triggers the ELM crash. Note that this behavior is atypical of the more usual MAST double-null-diverted discharges, in which the ELMS are not usually triggered by core MHD activity.

A. 2D BES imaging system

It is planned to implement a 2D BES imaging system on MAST with much greater capability than the existing trial system. For this it is intended to use a custom camera based on an 8×4 channel APD array sensor (Hamamatsu S8550) imaged with direct coupled optics to a 16×8 cm^2 region in the plasma. With such a 2D imaging system it should be possible to observe turbulence flow patterns and features such as geodesic acoustic mode (GAM) and zonal flows, as have been observed using the system installed on the DIII-D tokamak.[6] Using the BES simulation presented in Sec. III, which has been benchmarked against measurements made with the trial BES system, it is possible to predict the performance of this planned system. This will utilize a direct coupled imaging system with a periscopic collection optics consisting of a lens and steering mirrors inside the MAST vessel with an effective *f*-number of $F/10$ at the beam.

The planned system is intended to view the SS NBI heating beam which has a PINI source and the viewing geometry is to be very similar to that of the trial system shown in Fig. 1 but with a smaller separation of 2 cm between the eight radial viewing locations, which it will be possible to scan across the outer plasma radius from the magnetic axis to the outboard plasma edge. The higher beam energy from the

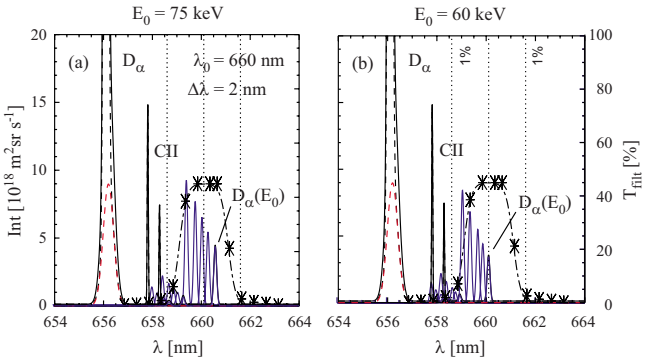

FIG. 14. (Color online) Predicted spectra for the proposed BES 2D imaging system for beam energies from the PINI source of (a) 75 keV and (b) 60 keV. The total emission is shown in black for a viewing radius of 0.9 m, and the contribution to the D_α beam emission from the three energy components for viewing radii of 0.9, 1.0, 1.1, 1.2, and 1.3 m is superimposed in blue. The transmission of the interference filter is shown in black dotted-dashed. The vertical dotted lines are the 1% transmission wavelengths and the central wavelength of the filter.

PINI of up to 75 keV compared to 50 keV from the ORNL source results in a larger Doppler shift of the D_α beam emission from a particular radial location, which facilitates blocking of the background emission from the CII lines to the red side of the unshifted D_α emission. Although the absence of interfering lines to the blue side of the D_α emission would favor a blueshifted view looking counter to the beam, the alignment of the *B*-field vectors with the lines of sight from a single location is not favorable across the full profile when viewing from this direction, thus degrading the spatial resolution to an unacceptable degree. There is also a lack of a suitable location for the optics on this side of the MAST vessel due to the presence of the beam dumps at this toroidal location.

Predicted spectra for the planned system are shown in Fig. 14 for beam energies of 60 and 75 keV, corresponding to injected powers of 1.8 and 2.5 MW, respectively. The Doppler shift of the beam emission depends on the viewing location because the projected component of the beam atom velocity along the line of sight decreases with increasing observation radius. Figure 14 shows the D_α emission lines from several locations, from the magnetic axis at ~ 0.9 m to the plasma periphery at ~ 1.3 m. From these figures it can be seen that a single three-cavity interference filter of 2 nm bandwidth is able to encompass the full energy E_0 component of the beam emission over this range of radii and beam energies. With a central wavelength of 660 nm the filter is also able to block the neighboring CII doublet effectively, these lines lying outside the wavelength region defined by the 1% transmission points of the filter bandpass envelope. The 160×80 mm^2 rectangular aperture filter is to be located at a 1:1 image of the beam in a telecentric region formed between a pair of lenses on either side.

The magnification of the optics from the detector to the beam is a factor 8.7, resulting in an *f*-number of $F/1.2$ at the detector. A high-quality Nikkor 50 mm, F1.2 camera lens is to be used for the final lens at the detector. The active area of the pixels of 1.6×1.6 mm^2 then defines the étendu of the collection optics as $\Delta\xi = \Delta A \Delta\Omega \sim 1.1 \times 10^{-6}$ m^2 sr, which is a factor 35 larger than that of the trial BES system. The pitch of the 8×4 APD sensor array of 2.3 mm defines the size of the imaged region of 16×8 cm^2 radially and vertically with a separation of 2 cm between adjacent channels. For predicting the performance of this system using the BES simulation we assume the same values for the transmission of the optics and the interference filter, the APD and preamplifier gains, and the amplifier bandwidth. With the PINI NBI source operating at 2.5 MW and 75 keV energy, the simulated photon count N_γ at the detectors is $\sim 3.2 \times 10^5$ for an observation radius of 1.2 m in the *L*-mode discharge 17068, which is two orders of magnitude larger than for the trial BES system observing the SW beam from the ORNL source at 1.2 MW. This would result in an output voltage from the existing preamplifier used in the trial system $V_{\text{out}} \sim 10$ V and SNR of 330 at 1 MHz bandwidth. The amplifier will however have to be optimized for the highest SNR at a reduced gain to operate with this much higher incident photon flux. With the correlation techniques allowing a sensitivity to fluctuations a factor of 3 below the statistical noise level to be achieved, the planned system should therefore be able to detect relative fluctuations in the D_α beam emission intensity at the 0.1% level. As mentioned above, with the lower divergence PINI source, the spatial smearing due to the finite extent of the emission volume is reduced to 2–3 cm, which is comparable to the channel separation of this planned system.

V. SUMMARY AND CONCLUSIONS

With the trial BES system currently installed on MAST it is possible to characterize relatively high-amplitude density turbulence at the periphery of *L*-mode plasmas and also to localize coherent MHD at the edge of *H*-mode plasmas. It is not possible, however, to characterize the core turbulence with confidence due to the limited signal level. Using these results, simulations of the BES system have also been benchmarked against experiment. This gives confidence in the predicted performance of a BES 2D imaging system, which is planned to be installed on MAST in 2009. This system is to utilize in-vessel optics with much increased étendu ($\times 35$) and should be able to detect fluctuations at the 0.1% level at 1 MHz bandwidth.

ACKNOWLEDGMENTS

This work was funded jointly by the United Kingdom Engineering and Physical Sciences Research Council and by the European Communities under the contract of Association between EURATOM and UKAEA. The views and opinions expressed herein do not necessarily reflect those of the European Commission.

[1] X. Garbet, P. Mantica, C. Angioni, E. Asp, Y. Baranov, C. Bourdelle, R. Budny, F. Crisanti, G. Cordey, L. Garzotti, N. Kirneva, D. Hogeweij, T. Hoang, F. Imbeaux, E. Joffrin, X. Litaudon, A. Manini, D. C. McDonald, H. Nordman, V. Parail, A. Peeters, F. Ryter, C. Sozzi, M. Valovic, T. Tala, A. Thyagaraja, I. Voitsekhovitch, J. Weiland, H. Weisen, A. Zabolotsky, and the JET EFDA Contributors, Plasma Phys. Controlled Fusion **46**, B557 (2004).
[2] A. J. Wootton, B. A. Carreras, H. Matsumoto, and K. McGuire, Phys. Fluids B **2**, 2879 (1990).
[3] A. Thyagaraja, P. J. Knight, M. R. de Baar, G. M. D. Hogeweij, and E.

Min, Phys. Plasmas **12**, 090907 (2005).
[4] P. C. Liewer, Nucl. Fusion **25**, 543 (1985).
[5] R. J. Fonck, P. A. Duperrex, and S. F. Paul, Rev. Sci. Instrum. **61**, 3487 (1990).
[6] G. R. McKee, R. J. Fonck, and D. K. Gubta, Rev. Sci. Instrum. **77**, F104 (2006).
[7] H. P. Summers, "Atomic data and analysis structure," JET Report No. JET-IR (94) 06, 1994.
[8] I. H. Hutchinson, Plasma Phys. Controlled Fusion **44**, 71 (2002).
[9] H. Anderson, M. G. von Hellermann, R. Hoekstra, L. D. Horton, A. C. Howman, R. W. T. Konig, R. Martin, R. E. Olson, and H. P. Summers, Plasma Phys. Controlled Fusion **42**, 781 (2000).
[10] N. J. Conway, P. G. Carolan, J. McCone, and M. J. Walsh, Rev. Sci. Instrum. **77**, 10F131 (2006).
[11] D. Dunai, J. Sarkosi, S. Zoletnik, Rev. Sci. Instrum. (unpublished).
[12] L. L. Lao, H. St John, R. D. Stambaugh, A. G. Kellman, and W. Pfeiffer, Nucl. Fusion **25**, 1611 (1985).
[13] W. W. Heidbrink, K. H. Burrell, Y. Luo, N A. Pablant, and E. Ruskov, Plasma Phys. Controlled Fusion **46**, 1855 (2004).
[14] M. W. Schafer, R. J. Fonck, G. R. McKee, and D. J. Schlossberg, Rev. Sci. Instrum. **77**, 053103 (2006).
[15] D. Dunai, A. R. Field, N. J. Conway, A. Thyagaraja, S. Zoletnik, and J. Sarkozi, 34th EPS Conference on Plasma Physics, Warsaw, Poland, 2007 (unpublished), Paper No. P5-082.
[16] S. Zoletnik, S. Fiedler, G. Kocsis, G. K. McCormick, J. Schweinzer, and H. P. Winter, Plasma Phys. Controlled Fusion **40**, 1399 (1998).
[17] A. Mazurenko, M. Porkolab, D. Mossessian, and J. A. Snipes, Phys. Rev. Lett. **89**, 225004 (2002).
[18] E. Belonohy, M. Hirsch, K. McCormick, G. Papp, G. Pokol, H. Thansen, A. Werner, S. Zoletnik, and W7-AS Team, 34th EPS Conference on Plasma Physics, Hersonissos, Greece, 2008 (unpublished), Paper No. P-2.034.
[19] S. Zoletnik, D. Dunai, A. R. Field, and A. Kirk, 35th EPS Conference on Plasma Physics, Hersonissos, Crete, 2008 (unpublished), Paper No. O4-O031.